for catalytic enantiocontrol in a broad range of organic triplet state reactions.

REFERENCES AND NOTES

1. Y. Inoue, *Chem. Rev.* **92**, 741–770 (1992).
2. R. Brimioulle, D. Lenhart, M. M. Maturi, T. Bach, *Angew. Chem. Int. Ed. Engl.* **54**, 3872–3890 (2015).
3. N. Hoffmann, *Chem. Rev.* **108**, 1052–1103 (2008).
4. T. Bach, J. P. Hehn, *Angew. Chem. Int. Ed. Engl.* **50**, 1000–1045 (2011).
5. C. K. Prier, D. A. Rankic, D. W. C. MacMillan, *Chem. Rev.* **113**, 5322–5363 (2013).
6. J. Du, K. L. Skubi, D. M. Schultz, T. P. Yoon, *Science* **344**, 392–396 (2014).
7. L. J. Rono, H. G. Yayla, D. Y. Wang, M. F. Armstrong, R. R. Knowles, *J. Am. Chem. Soc.* **135**, 17735–17738 (2013).
8. D. Uraguchi, N. Kinoshita, T. Kizu, T. Ooi, *J. Am. Chem. Soc.* **137**, 13768–13771 (2015).
9. D. A. Nicewicz, D. W. C. MacMillan, *Science* **322**, 77–80 (2008).
10. D. A. DiRocco, T. Rovis, *J. Am. Chem. Soc.* **134**, 8094–8097 (2012).
11. A. Studer, D. P. Curran, *Angew. Chem. Int. Ed. Engl.* **55**, 58–102 (2016).
12. C. Müller, A. Bauer, T. Bach, *Angew. Chem. Int. Ed. Engl.* **48**, 6640–6642 (2009).
13. R. Alonso, T. Bach, *Angew. Chem. Int. Ed. Engl.* **53**, 4368–4371 (2014).
14. M. M. Maturi, T. Bach, *Angew. Chem. Int. Ed. Engl.* **53**, 7661–7664 (2014).
15. N. Vallavoju, S. Selvakumar, S. Jockusch, M. P. Sibi, J. Sivaguru, *Angew. Chem. Int. Ed. Engl.* **53**, 5604–5608 (2014).
16. A. Tröster, R. Alonso, A. Bauer, T. Bach, *J. Am. Chem. Soc.* **138**, 7808–7811 (2016).
17. H. Guo, E. Herdtweck, T. Bach, *Angew. Chem. Int. Ed. Engl.* **49**, 7782–7785 (2010).
18. R. Brimioulle, T. Bach, *Angew. Chem. Int. Ed. Engl.* **53**, 12921–12924 (2014).
19. R. Brimioulle, H. Guo, T. Bach, *Chemistry* **18**, 7552–7560 (2012).
20. R. Brimioulle, T. Bach, *Science* **342**, 840–843 (2013).
21. R. Brimioulle, A. Bauer, T. Bach, *J. Am. Chem. Soc.* **137**, 5170–5176 (2015).
22. H. Wang, X. Cao, X. Chen, W. Fang, M. Dolg, *Angew. Chem. Int. Ed. Engl.* **54**, 14295–14298 (2015).
23. F. D. Lewis, D. K. Howard, J. D. Oxman, *J. Am. Chem. Soc.* **105**, 3344–3345 (1983).
24. F. D. Lewis, S. V. Barancyk, *J. Am. Chem. Soc.* **111**, 8653–8661 (1989).
25. L. Ruiz Espelt, I. S. McPherson, E. M. Wiensch, T. P. Yoon, *J. Am. Chem. Soc.* **137**, 2452–2455 (2015).
26. A. G. Amador, E. M. Sherbrook, T. P. Yoon, *J. Am. Chem. Soc.* **138**, 4722–4725 (2016).
27. Y. Norikane, H. Itoh, T. Arai, *J. Phys. Chem. A* **106**, 2766–2776 (2002).
28. K. Kalyanasundaram, *Coord. Chem. Rev.* **46**, 159–244 (1982).
29. Further details are provided in the supplementary materials.
30. The absolute configuration of the cycloadducts was determined by Riley oxidation of compound **9** to a crystalline derivative, which was unambiguously confirmed by single-crystal x-ray crystallography. Details are given in the supplementary materials.
31. The nature of this background process is poorly understood and is the subject of ongoing studies.
32. H. Cong, D. Ledbetter, G. T. Rowe, J. P. Caradonna, J. A. Porco Jr., *J. Am. Chem. Soc.* **130**, 9214–9215 (2008).
33. H. Cong, C. F. Becker, S. J. Elliott, M. W. Grinstaff, J. A. Porco Jr., *J. Am. Chem. Soc.* **132**, 7514–7518 (2010).
34. C. M. Elliott, R. A. Freitag, D. D. Blaney, *J. Am. Chem. Soc.* **107**, 4647–4655 (1985).
35. W. G. Herkstroeter, A. A. Lamola, G. S. Hammond, *J. Am. Chem. Soc.* **86**, 4537–4540 (1964).
36. E. N. Jacobsen, W. Zhang, M. L. Guler, *J. Am. Chem. Soc.* **113**, 6703–6704 (1991).

ACKNOWLEDGMENTS

We gratefully acknowledge experimental assistance from M. Arnold and M. Shea in obtaining near-IR luminescence spectra. We also thank J. Schomaker and M. Ju for access to chiral HPLC instrumentation. Experimental details for all studies reported in this paper are described in the supplementary materials. Funding for this project was provided by the NIH (GM09888). The computational resources were supported in part by NSF (CHE-0840494). T.R.B. acknowledges support from a NIH Chemical Biology Interface Training grant (T32 GM008505). T.R.B. conceived the project, conducted the optimization studies described in the supplementary materials, and performed the mechanistic studies. Z.D.M. collected the data reported in Table 1 and Fig. 2 and conducted the cyclic voltammetry studies. D.M.B. and T.R.B. performed the computational studies. I.A.G. collected and analyzed x-ray crystallographic data, which are available free of charge from the Cambridge Crystallographic Data Centre under accession number CCDC 1507886. All authors contributed to the writing and editing of the manuscript.

SUPPLEMENTARY MATERIALS

www.sciencemag.org/content/354/6318/1391/suppl/DC1
Materials and Methods
Supplementary Text
Figs. S1 to S7
Tables S1 to S18
References (*37*–*51*)
Spectral and Chromatographic Data

16 August 2016; accepted 18 November 2016
10.1126/science.aai8228

VOLCANOLOGY

Seismic constraints on caldera dynamics from the 2015 Axial Seamount eruption

William S. D. Wilcock,[1]* Maya Tolstoy,[2] Felix Waldhauser,[2] Charles Garcia,[1] Yen Joe Tan,[2] DelWayne R. Bohnenstiehl,[3] Jacqueline Caplan-Auerbach,[4] Robert P. Dziak,[5] Adrien F. Arnulf,[6] M. Everett Mann[3]

Seismic observations in volcanically active calderas are challenging. A new cabled observatory atop Axial Seamount on the Juan de Fuca ridge allows unprecedented real-time monitoring of a submarine caldera. Beginning on 24 April 2015, the seismic network captured an eruption that culminated in explosive acoustic signals where lava erupted on the seafloor. Extensive seismic activity preceding the eruption shows that inflation is accommodated by the reactivation of an outward-dipping caldera ring fault, with strong tidal triggering indicating a critically stressed system. The ring fault accommodated deflation during the eruption and provided a pathway for a dike that propagated south and north beneath the caldera's east wall. Once north of the caldera, the eruption stepped westward, and a dike propagated along the extensional north rift.

On land, seismic monitoring is one of the most widely used tools for characterizing volcanic cycles (*1*). Seismic monitoring of submarine volcanoes, which account for ≥80% of Earth's volcanism (*2*), is far more difficult because of the challenges of sustaining long-term observations and recovering instruments after an eruption (*3*). However, the volcanoes that form mid-ocean ridges erupt frequently with a uniform basaltic composition while also having shallow magmatic systems that can be imaged seismically at high resolution. These features make mid-ocean ridge volcanoes good targets for studies of eruption dynamics.

Calderas are important and complex features of many volcanoes. Most high-resolution constraints on the internal structure of the ring faults forming calderas come from geological studies of partially eroded calderas, and these have led to a long-standing debate about their orientation and configuration at depth (*4*, *5*). Earthquake observations at several locations support the existence of outward-dipping ring faults (*6*–*9*), but the only detailed seismic observation of the role of a ring fault in an eruption of a basaltic volcano comes from Bárdarbunga volcano, Iceland (*10*). There the lateral propagation of a dike sourced from a 12-km-deep magma chamber led to the collapse of a subglacial caldera with slip on a subvertical ring fault.

Axial Seamount is the most prominent volcanic feature on the Juan de Fuca mid-ocean ridge and is formed by the intersection of the ridge with the Cobb-Eickelberg hot spot. The summit at 1400-m depth below sea surface is characterized by a shallow caldera measuring 8.5 km by 3 km (Fig. 1A), which connects to rifts on the south and north flanks that form segments of the Juan de Fuca ridge. The caldera is underlain by a 14-km-long by 3-km-wide shallow magma and mush body with complex structure that is up to a kilometer thick, extends beyond both the northern and southern limits of the caldera, and

[1]School of Oceanography, University of Washington, Seattle, WA 98195, USA. [2]Lamont-Doherty Earth Observatory, Columbia University, Palisades, NY 10964, USA. [3]Department of Marine, Earth, and Atmospheric Sciences, North Carolina State University, Raleigh, NC 27695, USA. [4]Geology Department, Western Washington University, Bellingham, WA 98225, USA. [5]National Oceanic and Atmospheric Administration (NOAA), Pacific Marine Environmental Laboratory, Newport, OR 97365, USA. [6]Institute for Geophysics, Jackson School of Geosciences, University of Texas, Austin, TX 78758, USA.
*Corresponding author. Email: wilcock@uw.edu

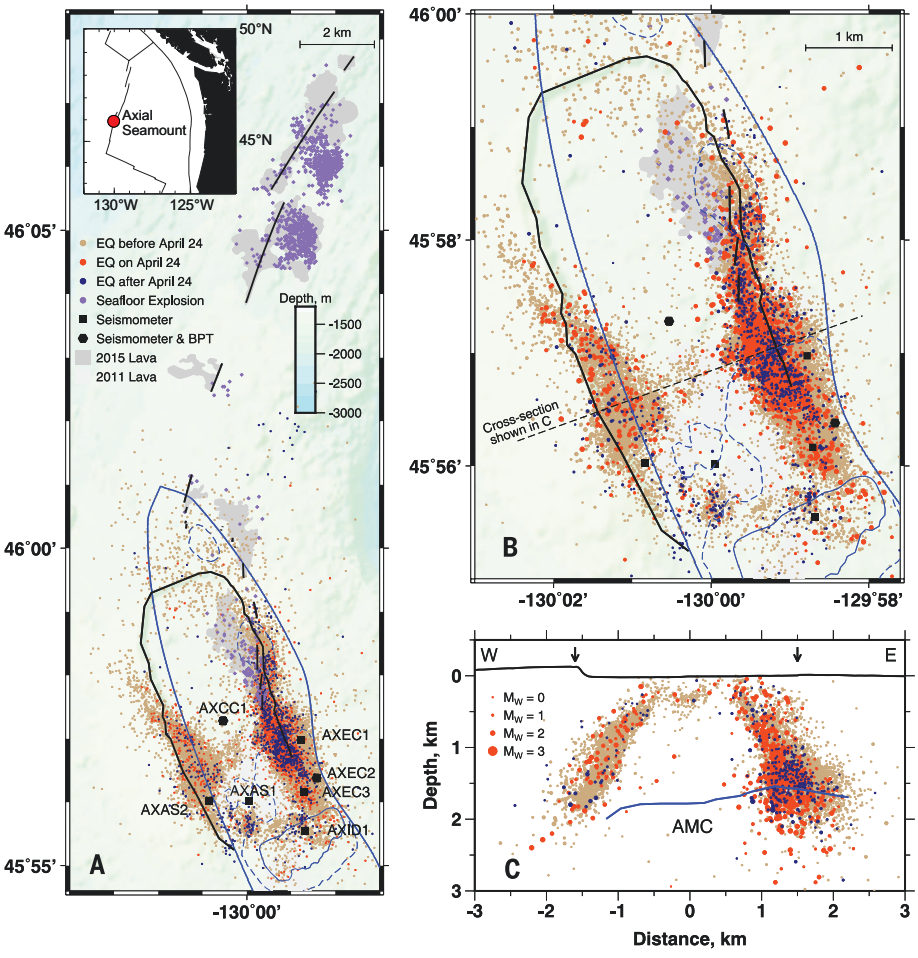

Fig. 1. Locations of earthquakes and seafloor explosions. (**A**) Bathymetric map showing the seismic network and colocated bottom-pressure and tilt (BPT) instruments, lava flows for the 2011 and 2015 eruptions (*21*), the distribution of 26,574 epicenters located with at least 12 arrival times by means of the double-difference technique, and seafloor explosions. The caldera rim (black line), eruptive fissures (black ticks), footprint of the magma chamber (blue solid line) (*11*), and depth contours for the magma chamber at depths of 1.25 km (faint blue line) and 1.5 km (dashed blue line) below the seafloor are also shown. The inset shows the location of Axial Seamount relative to plate boundaries (black lines) and land (black shading) in the northeast Pacific Ocean. (**B**) As in (A) but for the caldera region, with symbol sizes scaled by magnitude of earthquakes. (**C**) Vertical cross section across the caldera showing the projected locations of earthquakes within 0.5 km of the profile. Also shown is the roof of the axial magma chamber (AMC) (*11*). Arrows show the edges of the caldera.

is slightly offset to the east (*11*). Diking-eruptive events in the southeast caldera and south rift in 1998 and 2011 were documented with seafloor pressure sensors (*12*, *13*) and hydrophones (*14*, *15*). Although earthquake migration associated with dike propagation was observed for the 1998 eruption (*14*), earthquake depths could not be constrained for these eruptions. The expectation of future eruptions motivated the deployment in 2014 of a multidisciplinary real-time cabled observatory on Axial Seamount (*16*).

The cabled seismic network at the summit of Axial Seamount (Fig. 1) spans the southern half of the caldera, where the two prior recorded eruptions occurred, and comprises seven seismometers, two of which are colocated with hydrophones and bottom-pressure and tilt sensors (*17*). Seismic data are available starting in November 2014, with time-corrected data streaming from late January 2015. In the first year of operation, nearly 200,000 local earthquakes were detected, and they show a temporal distribution (Fig. 2) that is similar to prior seafloor eruptions (*3*, *15*). Earthquake rates increase from <500 day^{-1} to ~2000 day^{-1} leading up to the onset of the eruption on 24 April 2015, then decrease rapidly following the seismic crisis, reaching a background level within a month of 20 day^{-1}.

Leading up to the eruption, the earthquakes are strongly correlated with tides (Fig. 2), with rates of seismicity about six times greater during the lowest tides than the highest tides (fig. S1A). This pattern can be attributed to the faults unclamping when the ocean loading is at a minimum (*18*). There is no evidence that the triggering signal strengthens over the 5 months leading up to the eruption (fig. S2), but it weakens substantially after the eruption (supplementary text and fig. S1B), suggesting that it occurs primarily when the volcano is critically stressed (*19*).

In the 3 months prior to the eruption, ~60,000 earthquakes were located using double difference methods (*20*). Most are small with a median moment magnitude (M_w) of 0.1, and only 35 have $M_w \geq 2$. Earthquakes are concentrated beneath the east and west walls of the caldera (Fig. 1, fig. S3, and movie S1), with about five times as many beneath the east wall. In cross section (Fig. 1C), the earthquakes define outward-dipping fault zones extending from near the surface to ~2-km depth. These zones dip at 60° to 70°, with the dip decreasing slightly at shallow depths. Many of the remaining epicenters are located near the southern and northern ends of the caldera and in a diffuse band of shallow seismicity that extends across the caldera just south of 45°57′N at a location that coincides with the southern boundary of the 2015 eruption (*21*) and a northward transition from a melt rich to crystal mush magma chamber, as it was imaged in 2002 (*11*). The epicenters, thus, define a figure eight, with the southern ring more clearly depicted as a result of the station coverage (Fig. 1B and fig. S3B).

For 6 hours preceding the start of the eruption, coincident with high tide, bursts of 7- to 10-Hz tremor are observed (Fig. 3 and fig. S4C) across the network, but are not coherent enough to locate. Tremor is not observed in the weeks before, or after, the eruption, and is thus inferred to indicate magma movement within the magma chamber before crustal rupture. At ~04:20 UTC on 24 April, as the tremor ends, the rate and magnitude of seismicity start to increase. Over about 2 hours, the earthquake rate reaches a saturation level of 500 to 600 hour^{-1}, and the median magnitude increases from 0.5 to nearly 2, likely indicating the initiation of diking. At ~05:30, tilt sensors start to detect slight deformation, with more rapid deformation at ~06:15 (*17*), including a flip in polarity as the seismicity suggests a dike propagation past the central caldera station (movie S2). Bottom-pressure signals, indicating the start of deflation, were observed at ~06:00 to 06:30, with a notable increase in rate around ~07:15 (*17*) (movie S2). Seismic energy levels peak between 06:00 and 07:30 and then decrease progressively through the day (Fig. 3).

The cumulative distribution of hypocenters for the eruption is similar to that beforehand, with earthquakes concentrated near the east and west walls (Fig. 3). Of 31 earthquakes on 24 April with $M_w > 2.5$, all but one occurs on the eastern side, where the locations show a clear temporal pattern. Prior to 06:00 the seismicity along the east and west walls is north of 45°57′N, with most of it, including all earthquakes with $M_w \geq 2.0$, north of 45°58′N (figs. S5 and S6). Over about 1.5 hours, from 06:15 to 07:45, the locus of seismicity on the east wall migrates 2.5 km south to 45°56.5′N (Fig. 3B, fig. S5, and movie S2), consistent with the southward propagation of a dike. Up until 07:00, the earthquakes align closely with the north-south

strike of southernmost eruptive fissures (*21*), suggesting that the fissure might be opening. After 07:00, they follow the strike of the east wall. Earthquakes for the remainder of the crisis occur beneath the whole east wall and on the west wall but are concentrated on the east wall south of the 2015 eruptive vents between 45°56.5′N and 45°57.5′N, where they are presumably associated with deflation.

Starting at 08:01 on 24 April, the seismic network recorded ~37,000 impulsive events (fig. S4B) consistent with sound sources on the seafloor that propagate through the water column and are detected on the seismometers as a train of reverberations. Unlike the earthquakes, the times of explosions are not correlated with tides (fig. S7). These events are spatially closely associated with all the new lava flows (*21*) (Fig. 1A). The first impulsive event was observed within the caldera with events then commencing successively on the flows to the north.

Impulsive acoustic signals from the seafloor associated with active lava flows have been reported from several locations (*22*–*25*) and in deep-water locations have generally been attributed to the expansion of magmatic gases in Strombolian eruptions (*24*, *26*). The presence of pyroclastic ash deposits associated with the 2015 Axial eruption (*21*), coupled with the high CO_2 contents of some lavas from prior eruptions (*27*), is consistent with the occurrence of similar explosions at Axial. However, the lava flows are also covered with numerous pits, which are interpreted as small steam explosions and may be the dominant source of explosive acoustic signals at this location (*21*).

Whatever the mechanisms, the explosive signals start soon after magma reaches the seafloor (*25*). The first detected explosion within the caldera occurred within an hour of the onset of rapid deflation, and earlier explosions may have been missed in the noise of the seismic crisis. The onset times on the north rift suggest that the dike propagated at a speed of 0.55 m/s (Fig. 3). This is at the upper end of speeds observed in Iceland, Afar, and the Gulf of Aden (*28*–*30*) and faster than the speed of 0.23 m/s observed well down rift for the 1998 eruption of Axial Seamount (*14*) and thus is consistent with the rapid deflation observed for this eruption (*17*). The summit network detected no earthquakes associated with dike propagation along the north rift, a result of a shadowing effect from the elongated magma chamber and high noise levels from nearby earthquakes. However, northward dike propagation is supported by observations on a single seismic station 20 km southeast of the caldera (fig. S8). We infer that the dike started northwards around 07:15 at the outset of rapid deflation, taking <2 hours to reach the site of the first explosion on the north rift at 09:04. Explosions near the northern end of the 2015 lava flows continued until 21 May (fig. S7), which coincides with the time the caldera started to reinflate (*17*), lending further support to a mechanism that links the explosions to fresh lava reaching the seafloor and showing that the plumbing system of the caldera links to the north rift dike.

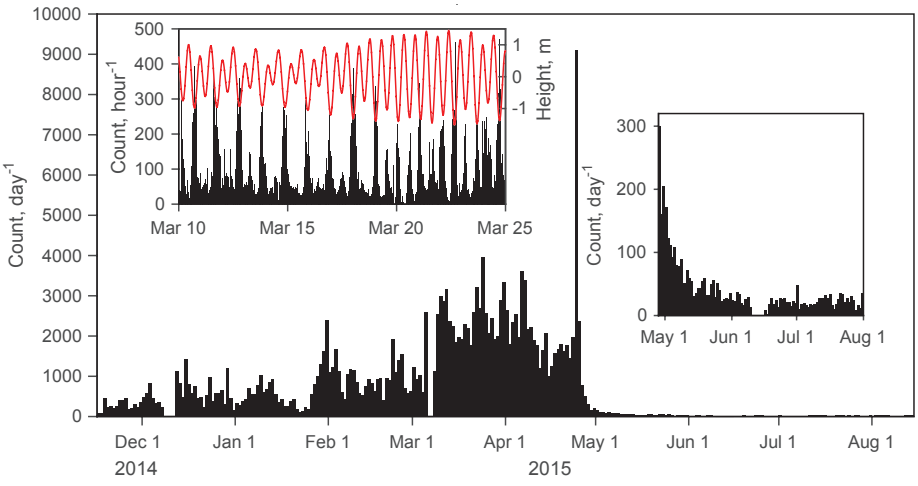

Fig. 2. Histogram of earthquake detections for 9 months spanning the 2015 eruption. (**Right inset**) Magnification of the period after the eruption. (**Left inset**) Histogram of hourly detections for 15 days in March with ocean tides superimposed. Gaps in the histogram in December, March, and June are intervals for which data are unavailable

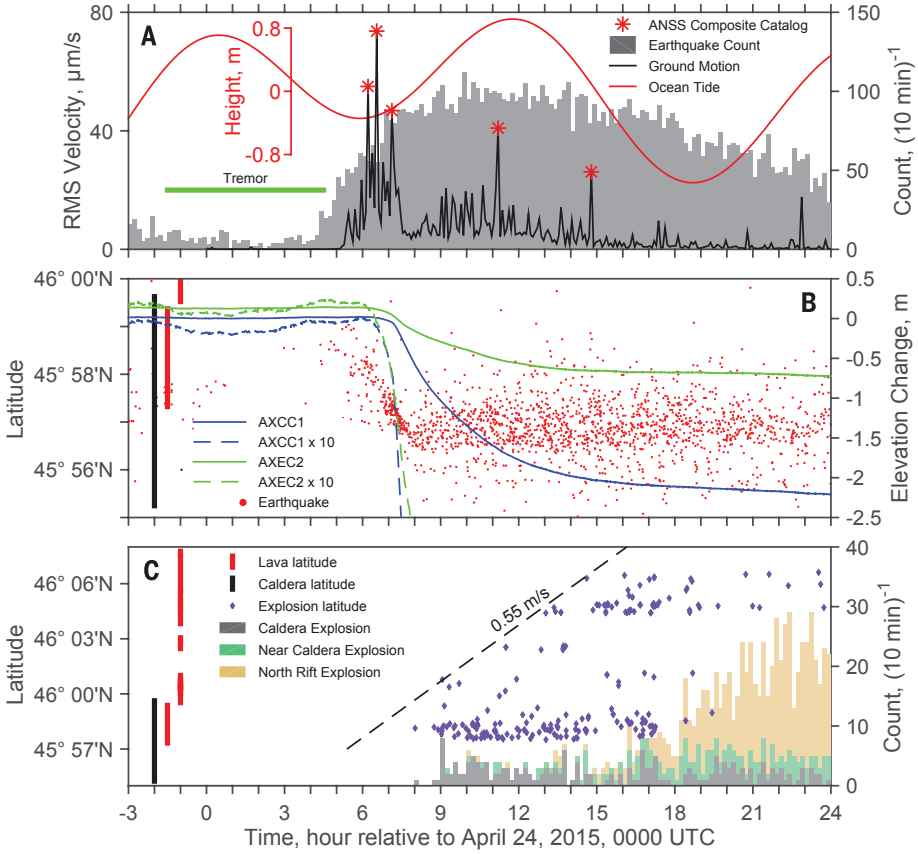

Fig. 3. Chronology for the 24 April 2015 eruption. (**A**) Histogram of earthquake counts, root mean square ground motion at station AXCC1 in the center of the caldera averaged over 5 min, times of earthquakes detected on land and included in the Advanced National Seismic System (ANSS) composite catalog, and ocean tides height. (**B**) Latitude of earthquakes beneath the east wall and the change in seafloor elevation recorded at stations AXCC1 and AXEC1 (*17*). (**C**) Histogram of explosions within the caldera and on the north rift and plot of latitudes for a subset of explosions.

The fault structure in the caldera is consistent with analog models obtained from sandbox simulations of caldera collapse due to underpressure (*31*–*33*), which show that with sufficient subsidence, an outward-dipping ring fault forms first, followed by a peripheral inward-dipping

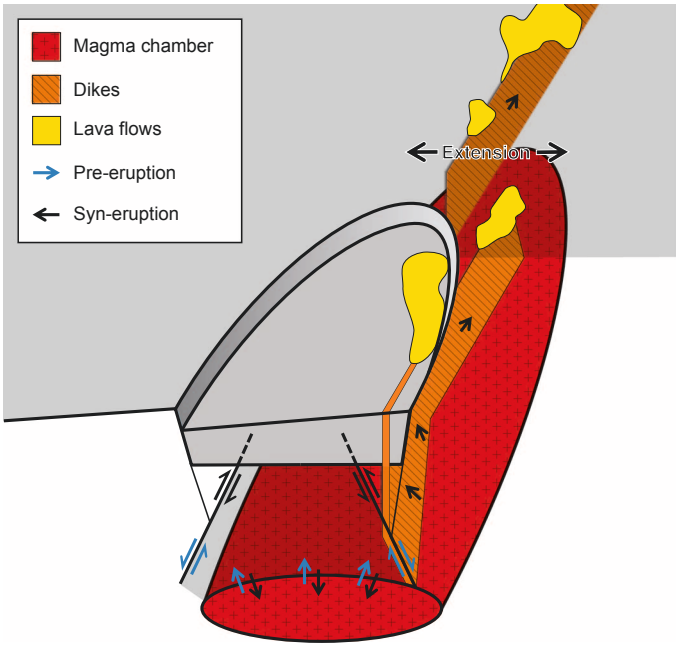

Fig. 4. Cartoon illustrating the dynamics of the caldera and emplacement of dikes. Normal faulting on the outward-dipping ring fault accommodates magma chamber inflation (blue arrows). This fault motion reverses while dikes are emplaced and the magma chamber deflates (black arrows).

ring fault. At Axial Seamount, the outward-dipping normal fault zones were active both during inflation and syn-eruptive deflation and they project to the caldera floor ~0.75 km inward from walls (Fig. 1C). We infer that the caldera walls are formed by a second ring of inward-dipping normal faults, features that appear to be visible in seismic images (*11*), that either deformed aseismically during this volcanic cycle or were not reactivated. The analog models predict that the outward-dipping faults nucleate near the outer margins of the magma chamber. The separation of the fault zones that we observe is consistent with the 3- to 4-km width of the magma chamber (*11*), but the magma chamber is offset about 0.5 to 1 km east of the caldera. We speculate that the magma chamber may have migrated slightly eastward with the Cobb-Eickelberg hot spot melting anomaly since the caldera formed. Comparisons of natural calderas with analog models suggest that the formation of two sets of ring structures requires a ratio of caldera diameter to subsidence less than ~14 (*34*). For Axial Seamount, the maximum height of the walls (160 m) and short- and long-axis dimensions yield ratios of 20 and 50, respectively. However, the caldera may have undergone substantial magmatic infilling since its formation, implying that the ratios may have originally been lower.

The caldera substantially modulates the eruption. The north rift intersects the center of the north rim, but within the caldera and just to the north, the eruptive fissures are offset 2 km to the east (*21*). We infer that beneath the caldera, a dike exited the side of the pressurized magma chamber where extensional stresses are highest (*35*) and followed a path of weakness coinciding with the eastern ring fault zone (Fig. 4). The southward migration of earthquakes and change in the north-south tilt signal at the caldera center (*17*) (movie S2) are consistent with the propagation of a dike that stalled upon reaching the northern limit of the 1998 and 2011 eruptions. Almost certainly at the same time, when the seismic noise levels were too high to detect earthquakes outside the network, the dike also propagated north, essentially extending the trend of the Axial south rift. Once north of the caldera, but still within the footprint of the Axial magma chamber, diking stepped westward into the extensional north rift, forming a second dike (Fig. 4). Although we cannot rule out that a single westward-stepping dike generated both the eruptions along the east wall of the caldera and the eruptions along the north rift (*21*), we prefer a model with two dikes tapping separate sections of the magma chamber. The eruption of north rift lavas with more evolved compositions (lower MgO) compared to the eastern caldera flows (*21*) is consistent with the dikes feeding these flows being sourced from different portions of the magma reservoir (Fig. 4), and the distribution of eruptive fissures and lava flows (Fig. 1A) are consistent with an overlapping spreading center. Injection of magma into the outward-dipping ring fault can be accommodated by the subsidence of the central block, but broadly distributed subsidence associated with deflation will increase horizontal compressive stresses above the caldera. This likely explains why the caldera eruption was limited in volume and most of the magma was injected along the rift (*21*).

At time scales on the order of a year, eruptions at Axial Seamount appear to be predictable based on a critical level of inflation (*16*). Similarly, it is clear from this study and prior work (*3*, *14*, *19*) that high and increasing microearthquake rates and strong tidal triggering also foreshadow eruptions on mid-ocean ridges. On shorter time scales of days to weeks, it is not clear if there are notable geophysical precursors. The 2015 Axial eruption was not preceded by a short-term increase in tidal triggering (fig. S2), and earthquake rates decreased noticeably in the 2 weeks beforehand (Fig. 2). The only precursor appears to be tremor observed a few hours ahead of the seismic crisis (Fig. 3A). For future eruptions at Axial, the development of the hydrothermal portion of the cabled observatory (*16*) will provide additional tools to search for precursory signals originating near the magma-hydrothermal interface.

The 2015 eruption of Axial Seamount bears many similarities to diking events on both submarine (*3*, *14*, *15*, *25*, *30*) and subaerial (*10*, *28*, *29*) spreading centers, although in areas of thicker lithosphere, rifting episodes lead to larger earthquakes and often involve multiple dikes (*28*–*30*) because the magma chamber must refill multiple times to accommodate the spreading (*36*). On land, in Iceland and Afar, the combination of seismic and geodetic data shows that the propagation of dikes over tens of kilometers is accompanied by subsidence above a deflating crustal magma chamber (*10*, *28*, *29*) and at Bárdarbunga volcano by the collapse of a caldera (*10*). Because the Axial seismic network is compact and the ring faults are shallow, we are able to show that the outward-dipping inner ring fault also accommodates inflation prior to eruption. At Bárdarbunga volcano (*10*) and several other calderas (*37*), collapse occurs well after the onset of magma withdrawal, but at Axial, the onset of deflation and seismicity are coincident, supporting the inference that the dynamics of calderas are influenced by the depth of the magma chamber and the strength of preexisting ring faults (*37*).

REFERENCES AND NOTES

1. V. M. Zobin, *Introduction to Volcanic Seismology* (Elsevier, Waltham, MA, ed. 2, 2012).
2. J. A. Crisp, *J. Volcanol. Geotherm. Res.* **20**, 177–211 (1984).
3. M. Tolstoy *et al.*, *Science* **314**, 1920–1922 (2006).
4. C. G. Newhall, D. Dzurisin, *U.S. Geol. Surv. Bull.* **1855** (1988).
5. A. Geyer, J. Marti, *Front. Earth Sci.* **2**, 1–13 (2014).
6. J. Mori, C. McKee, *Science* **235**, 193–195 (1987).
7. J. Mori *et al.*, in *Fire and Mud: Eruptions and Lahars of Mount Pinatubo, Philippines*, C. G. Newhall, R. S. Punongbayan, Eds. (Univ. of Washington Press, Seattle, 1996), pp. 335–350.
8. G. Ekström, *Earth Planet. Sci. Lett.* **128**, 707–712 (1994).
9. S. Prejean, A. Stork, W. Ellsworth, D. Hill, B. Julian, *Geophys. Res. Lett.* **30**, 2247 (2003).
10. M. T. Gudmundsson *et al.*, *Science* **353**, aaf8988 (2016).
11. A. F. Arnulf *et al.*, *Geology* **42**, 655–658 (2014).
12. C. G. Fox, W. W. Chadwick Jr., R. W. Embley, *Nature* **412**, 727–729 (2001).
13. W. W. Chadwick Jr., S. L. Nooner, D. A. Butterfield, M. D. Lilley, *Nat. Geosci.* **5**, 474–477 (2012).
14. R. P. Dziak, C. G. Fox, *Geophys. Res. Lett.* **26**, 3429–3432 (1999).
15. R. P. Dziak *et al.*, *Nat. Geosci.* **5**, 478–482 (2012).
16. D. S. Kelley, J. R. Delaney, S. K. Juniper, *Mar. Geol.* **352**, 426–450 (2014).
17. S. L. Nooner, W. W. Chadwick Jr., *Science* **354**, 1399–1403 (2016).
18. W. S. D. Wilcock, *Geophys. Res. Lett.* **28**, 3999–4002 (2001).
19. D. F. Stroup, D. R. Bohnenstiehl, M. Tolstoy, F. Waldhauser, R. T. Weekly, *Geophys. Res. Lett.* **34**, L15301 (2007).
20. F. Waldhauser, W. L. Ellsworth, *Bull. Seismol. Soc. Am.* **90**, 1353–1368 (2000).
21. W. W. Chadwick Jr. *et al.*, *Geophys. Res. Lett.* 10.1002/2016GL071327 (2016).
22. J. Caplan-Auerbach, F. Duennebier, *Geochem. Geophys. Geosyst.* **2**, 1024 (2001).
23. V. Schlindwein, C. Riedel, *Geochem. Geophys. Geosyst.* **11**, Q01002 (2010).

24. R. P. Dziak *et al.*, *Geophys. Res. Lett.* **42**, 1480–1487 (2015).
25. Y. J. Tan, M. Tolstoy, F. Waldhauser, W. S. D. Wilcock, *Nature* 10.1038/nature20116 (2016).
26. R. A. Sohn *et al.*, *Nature* **453**, 1236–1238 (2008).
27. C. Helo, M.-A. Longpré, N. Shimizu, D. A. Clague, J. Stix, *Nat. Geosci.* **4**, 260–263 (2011).
28. T. J. Wright *et al.*, *Nat. Geosci.* **5**, 242–250 (2012).
29. F. Sigmundsson *et al.*, *Nature* **517**, 191–195 (2015).
30. A. Ahmed *et al.*, *Geophys. J. Int.* **205**, 1244–1266 (2016).
31. O. Roche, O. T. H. Druitt, O. Merle, *J. Geophys. Res.* **105**, 395–416 (2000).
32. B. Kennedy, J. Stix, J. W. Vallance, Y. Lavallee, M.-A. Longpré, *Geol. Soc. Am. Bull.* **116**, 515–524 (2004).
33. S. Buchardt, T. R. Walter, *Bull. Volcanol.* **72**, 297–308 (2010).
34. V. Acocella, *Earth Sci. Rev.* **85**, 125–160 (2007).
35. A. Gudmundsson, L. B. Marinoni, J. Marti, *J. Volcanol. Geotherm. Res.* **88**, 1–13 (1999).
36. W. R. Buck, P. Einarsson, B. Brandsdóttir, *J. Geophys. Res.* **111**, B12404 (2006).
37. L. Michon, F. Massin, V. Famin, V. Ferrazzini, G. Roult, *J. Geophys. Res.* **116** (B3), B03209 (2011).

ACKNOWLEDGMENTS

The seismic data used for this study are archived at the Incorporated Research Institutions for Seismology Data Management System and the Ocean Observatories Initiative (OOI) Data Portal. The earthquake catalogs are archived in the Interdisciplinary Earth Data Alliance Marine Geoscience Data System (DOI: 10.1594/IEDA/323843). This work was supported by the National Science Foundation under awards OCE-1536219, OCE-1536320, OCE-1635276, OCE-1357076, and DGE-1256082. The seismic network was installed and is operated by the OOI Cabled Array team, led by J. Delaney and D. Kelley. This paper is Pacific Marine Environmental Laboratory contribution no. 4522.

SUPPLEMENTARY MATERIALS

www.sciencemag.org/content/354/6318/1395/suppl/DC1
Materials and Methods
Figs. S1 to S11
Movies S1 and S2
References (*38*–*40*)

15 July 2016; accepted 28 October 2016
10.1126/science.aah5563

VOLCANOLOGY

Inflation-predictable behavior and co-eruption deformation at Axial Seamount

Scott L. Nooner[1]* and William W. Chadwick Jr.[2]

Deformation of the ground surface at active volcanoes provides information about magma movements at depth. Improved seafloor deformation measurements between 2011 and 2015 documented a fourfold increase in magma supply and confirmed that Axial Seamount's eruptive behavior is inflation-predictable, probably triggered by a critical level of magmatic pressure. A 2015 eruption was successfully forecast on the basis of this deformation pattern and marked the first time that deflation and tilt were captured in real time by a new seafloor cabled observatory, revealing the timing, location, and volume of eruption-related magma movements. Improved modeling of the deformation suggests a steeply dipping prolate-spheroid pressure source beneath the eastern caldera that is consistent with the location of the zone of highest melt within the subcaldera magma reservoir determined from multichannel seismic results.

Successful volcanic eruption forecasting is traditionally based on short-term (minutes to hours) increases in seismicity, surface deformation, or both during the time that magma is already moving toward the surface (*1*, *2*). Successful forecasts made days to weeks in advance are much rarer because the patterns of geophysical signals are generally not clear or repeatable enough. However, some notable successes at volcanoes such as Mount St. Helens and in Iceland have been documented (*3*, *4*). Seven months in advance of an April 2015 eruption at Axial Seamount, we made a successful forecast that it would occur within a 15-month time window, on the basis of long-term deformation monitoring. The deformation measured during the 2015 eruption also provides important constraints on the location and depth of magma reservoirs and conduits.

[1]University of North Carolina Wilmington, Wilmington, NC 28403, USA. [2]Oregon State University/Cooperative Institute for Marine Resources Studies, Hatfield Marine Science Center, Newport, OR 97365, USA.
*Corresponding author. Email: nooners@uncw.edu

Axial Seamount is a heavily instrumented submarine volcano that is part of the Ocean Observatories Initiative (OOI) Cabled Array (*5*, *6*). Axial Seamount is distinguished from other submarine volcanoes in that it has a long-term volcano deformation time series that spans three eruptions. A combination of bottom pressure recorders (BPRs) and mobile pressure recorders (MPRs) (*7*–*11*) provided measurements of vertical deformation from 2000 to 2015. Both methods use changes in the overlying water pressure to detect vertical displacements of the seafloor with a resolution of ~1 cm. BPRs record continuously to capture sudden events (such as eruptions) over minutes to days, but these instruments are not ideal for longer-term measurements because of sensor drift. MPR campaign-style surveys require a remotely operated vehicle (ROV) to deploy the instrument at seafloor benchmarks (fig. S1) and, after correcting for sensor drift, can document gradual deformation over months to years (*9*, *10*). MPR data can constrain BPR drift where the two are colocated. Autonomous, battery-powered BPRs have been used at Axial since the mid-1980s (*12*, *13*) and, in September 2014, the OOI Cabled Array began providing real-time data from three BPR-tilt instruments (*5*, *6*). At the time of the 2015 eruption, three autonomous BPRs, three cabled BPRs, and 10 MPR benchmarks were deployed at Axial (Fig. 1 and fig. S2).

After the 2011 eruption at Axial Seamount (*14*), a time- or inflation-predictable model was proposed in which the volcano erupts at or near a threshold level of inflation (*15*, *16*). The 2015 eruption provided a test for this model and its usefulness in forecasting. The average linear rate of inflation measured at the caldera center between 2000 and 2010 was 15 ± 0.2 cm/year (Fig. 2), with higher rates measured in the months after the 1998 eruption and before the eruption in 2011 (*14*). After 2011, we initially expected the next eruption to occur in 2018 if the pattern of deformation repeated itself (*14*). However, from continued monitoring we found that the rate of inflation increased substantially after the 2011 eruption. We observed that the average inflation rate at the caldera center was 61 ± 1.4 cm/year between August 2011 and September 2013 (Fig. 2). A marked increase in the magma supply may explain the fourfold increase over the 2000–2010 inter-eruption rate (*11*). Continuation of this higher rate of inflation during 2013–2014 was observed after a Monterey Bay Aquarium Research Institute autonomous underwater vehicle (AUV) collected repeat high-resolution bathymetry (*17*) and with data recovered from a prototype self-calibrating BPR (*18*) in August 2014. Thus, in September 2014, we revised our forecast that Axial would erupt sometime during 2015 (*19*, *20*). The expected eruption began on 24 April 2015, detected in real time by the OOI Cabled Array (*21*).

This long-term forecast was unusually successful for any volcano (*1*, *2*). The level of inflation as the 2015 eruption began was only 30 cm higher than in 2011 (Fig. 2). This observation supports the model of a pressure threshold in the shallow magma reservoir above which diking events are triggered, but it also suggests that the threshold may increase with time because of accumulating tectonic stress, as observed in Iceland and Ethiopia (*22*, *23*). Nevertheless, the volcanic system at Axial may be unusually repeatable due to the continuous magma supply and the thin ocean crust in a mid-ocean ridge setting. The increase in magma supply rate documented by the inflation data led to a marked decrease in the eruption

Seismic constraints on caldera dynamics from the 2015 Axial Seamount eruption

William S. D. Wilcock, Maya Tolstoy, Felix Waldhauser, Charles Garcia, Yen Joe Tan, DelWayne R. Bohnenstiehl, Jacqueline Caplan-Auerbach, Robert P. Dziak, Adrien F. Arnulf and M. Everett Mann (December 15, 2016)

Science **354** (6318), 1395-1399. [doi: 10.1126/science.aah5563]

Editor's Summary

Volcano monitoring goes into the deep

Axial Seamount is a large and active submarine volcano along the Juan de Fuca midocean ridge off the coast of the western United States. Eruptions in 1998 and 2011 were followed by periods of magma recharge, making it an ideal location to include in the Ocean Observatories Initiative Cabled Array. Wilcock *et al.* present real-time seismic data from the most recent eruption in April 2015 that allow the tracking of magma before and during eruption. Nooner and Chadwick show that eruptions are predictable on the basis of deformation data. As magma pools underneath it, Axial Seamount inflates and erupts when the inflation hits a threshold. Both studies elucidate the dynamics of submarine volcanoes, which vastly outnumber their aboveground counterparts.

Science, this issue p. 1395, p. 1399

Science (print ISSN 0036-8075; online ISSN 1095-9203) is published weekly, except the last week in December, by the American Association for the Advancement of Science, 1200 New York Avenue NW, Washington, DC 20005.